

See discussions, stats, and author profiles for this publication at: <https://www.researchgate.net/publication/263978965>

Nano-PtPd Cubes on Graphene Exhibit Enhanced Activity and Durability in Methanol Electrooxidation after CO Stripping-Cleaning

ARTICLE in THE JOURNAL OF PHYSICAL CHEMISTRY C · JANUARY 2013

Impact Factor: 4.77 · DOI: 10.1021/jp3116726

CITATIONS

64

READS

76

4 AUTHORS, INCLUDING:



Lu Yizhong

Chinese Academy of Sciences

19 PUBLICATIONS 880 CITATIONS

SEE PROFILE



Haibin Wu

University of California, San Diego

5 PUBLICATIONS 177 CITATIONS

SEE PROFILE



Wei Chen

Chinese Academy of Sciences

876 PUBLICATIONS 13,896 CITATIONS

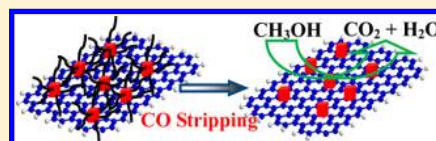
SEE PROFILE

Nano-PtPd Cubes on Graphene Exhibit Enhanced Activity and Durability in Methanol Electrooxidation after CO Stripping–Cleaning

Yizhong Lu,^{†,‡} Yuanyuan Jiang,^{†,‡} Haibin Wu,[†] and Wei Chen^{*,†}[†]State Key Laboratory of Electroanalytical Chemistry, Changchun Institute of Applied Chemistry, Chinese Academy of Sciences, Changchun 130022, Jilin, China[‡]Graduate School of the Chinese Academy of Sciences, Beijing 100039, China

S Supporting Information

ABSTRACT: Graphene-supported PtPd alloy nanocubes (PtPd/RGO) were synthesized via a facile and versatile one-pot hydrothermal synthetic strategy, which proved to be a universal technique for preparing other graphene-supported alloy nanocrystals. In acidic electrolyte, the PtPd/RGO composites exhibited much enhanced electrocatalytic activity toward methanol oxidation compared to the unsupported PtPd alloy nanocubes with a similar size and shape, and the commercial Pt/C catalyst. More interestingly, we found that CO stripping is an efficient method to remove the surfactants wrapped on the particle surface and thus enhance the electrocatalytic performance of the Pt-based nanocrystals. After CO stripping treatment, the PtPd/RGO composites exhibited a much more negative onset potential of methanol oxidation than those of the unsupported PtPd alloy nanocubes and the commercial Pt/C catalyst. Moreover, the treated PtPd/RGO displayed a mass-specific methanol oxidation activity of 198 mA/mg_{Metal} at 0.62 V (vs Ag/AgCl), nearly 3.14 times higher than those of the unsupported PtPd alloy nanocubes (63 mA/mg_{Metal}) and the commercial Pt/C catalyst (64 mA/mg_{Metal}). On the other hand, the PtPd/RGO exhibited much higher stability during the methanol electrooxidation with almost no loss of the electrochemical active surface area (ECSA) and activity after 1000 electrochemical cycles. On the contrary, the unsupported PtPd nanocubes and the commercial Pt/C catalyst lost 8.5% and 25.7% of their initial ECSA, and 6.2% and 20.6% of the initial peak current after 1000 cycles of methanol oxidation reaction. The excellent stability of the PtPd/RGO can also be reflected from the fact that the morphology, size, and dispersity of the PtPd nanocubes exhibited no significant change after 1000 potential cycles.



1. INTRODUCTION

Because of the high power density, high energy-conversion efficiency, and zero or low emission of pollutants, fuel cells, such as proton-exchange membrane fuel cells (PEMFCs), direct methanol fuel cells (DMFCs), and alkaline fuel cells (AFCs), have attracted increasing attention over the past decades.¹ For fuel cells, platinum has been widely used as the electrocatalyst because it has the highest catalytic activity among the catalysts for electrooxidation of small organic fuels on the anode and oxygen reduction on the cathode.² However, two major disadvantages have been revealed by using Pt as an anode catalyst. First, the catalyst surface can be heavily poisoned by the strong adsorption of CO intermediates produced during the oxidation of organic fuels, thus lowering the catalytic performance.³ Second, the high cost and limited supply of Pt largely hinder the wide commercialization of fuel cells. To reduce the overall cost and improve the tolerance to the self-poisoning of electrocatalysts, Pt-based alloy nanocrystals with controlled surface structures and compositions have been extensively investigated in recent years.⁴

For nanoelectrocatalysts, the catalytic efficiency, selectivity, and durability are highly dependent on the size, shape, composition, structure (solid, hollow, or porous), and the dispersity of the catalyst nanoparticles.^{2a,c,5} More interestingly, it has also been found that alcohol oxidation is very sensitive to the surface electronic structure and the arrangement of Pt

atoms of the catalysts. Therefore, it would be of great significance to develop a facile method to synthesize well-dispersed Pt-based alloy nanoparticles with specific morphologies and a narrow size distribution. To date, PtPd bimetallic nanocrystals with various shapes have been synthesized by using different methods.⁶ Pt-on-Pd alloy nanocrystals with star-shaped decahedrons, nanodendrites, and truncated triangular nanoplates have been successfully synthesized mainly by using either successive coreduction of Pt and Pd precursors or seed-mediated growth strategies.⁷ Although recent progress has allowed the synthesis of Pt–Pd bimetallic alloy nanocrystals with various shapes through different techniques, the design and synthesis of highly active Pt–Pd alloy nanoparticles with desirable structures using a one-pot method and exploring their properties still remain challenging.

Nowadays, the state-of-the-art commercial catalysts are usually prepared by dispersing Pt nanoparticles (2–5 nm) on carbon supports. However, the severe corrosion and oxidation of the carbon support in the harsh operating environment would lead to the quick loss of the electrocatalytic activity of the catalysts.⁸ Thus, the catalyst supports play an important role in controlling the catalytic properties. Earlier studies have

Received: November 27, 2012

Revised: January 6, 2013

Published: January 14, 2013

shown that a good catalyst support material should have a high surface area, a strong affinity toward the catalyst particles to immobilize them, while also ensuring their good dispersion, a high electrical conductivity to promote fast electron transfer in redox reactions, and high chemical stability under the operating conditions to maintain a stable structure. More recently, graphene has attracted unusual attention due to its outstanding physical and chemical properties and potential wide applications.⁹ The high theoretical surface areas ($\sim 2600 \text{ m}^2/\text{g}$), excellent electric conductivity, good chemical and environmental stability, strong mechanical strength, and strong adhesion to catalyst particles have made graphene highly desirable for use as a 2-D catalyst support.¹⁰ However, two major hurdles remain in developing large-scale graphene-supported catalyst systems. The first one is to obtain solution-processable individual graphene sheets, and the second one is to obtain well-dispersed nanoparticles decorated on graphene.

Recently, Pd-based catalysts have become a hot topic of interest because of their lower cost and greater resistance to CO in comparison with Pt catalysts in polymer electrolyte membrane fuel cells.¹¹ Studies based on first-principles calculations indicated that Pd could interact with and bind more strongly to graphene because more interaction states and transmission channels are generated between them and because Pd tends to grow into three-dimensional structures on graphene surfaces.¹² These studies provide a hint that graphene could be an ideal substrate for growing and anchoring Pd-based nanoparticles for high-performance electrocatalysts. However, manipulating the shape of alloy nanostructures on graphene is not a straightforward task due to the difficulties involved in controlling the nucleation and growth of nanostructures in the presence of various metal precursors with different reduction kinetics.

Herein, we report a facile and versatile synthetic strategy that allows the one-pot fabrication of water-soluble and uniform single-crystalline PtPd alloy nanocubes supported on reduced graphene oxide nanosheets (PtPd/RGO). This method could also be used to synthesize other water-soluble Pt- or Pd-based alloy nanocrystals supported on RGO with desirable morphologies. The as-synthesized PtPd/RGO composites exhibited excellent electrocatalytic activity and stability toward the methanol oxidation. Moreover, the effects of the graphene support on the catalytic activity and stability of PtPd nanocubes were also investigated by comparing the catalytic performance of PtPd/RGO with that of unsupported PtPd nanocubes with a similar size and shape.

On the other hand, nanoparticles with controlled sizes, shapes, and compositions are usually capped with organic ligands (surfactants), which will heavily reduce their surface electrocatalytic activity. Therefore, from the viewpoint of the application of nanoparticles in catalysis, it is critical to establish a proper procedure for surfactant removal and surface cleaning without inducing particle size and morphology change. In the past years, various methods have been applied to remove oleylamine or other commonly used surfactants from the particle surface, including thermal annealing,¹³ acetic acid washing,¹⁴ plasma cleaning,^{2d} and UV-ozone irradiation.^{2b,c,15} In this paper, we found for the first time that CO stripping is an efficient method to clean or remove the surfactants and thus to enhance the catalytic activity of nanoparticles. The present study shows that the electrocatalytic performance of PtPd nanocubes supported on graphene, including the electrochemically active surface area (ECSA), catalytic activity (mass- and

area-specific activities), and stability, increased greatly after the CO stripping treatment. Compared to the previously reported methods to activate surfactant-protected nanoparticle catalysts, the CO stripping method shown here is simple, efficient, and needs only several minutes at room temperature. Overall, the present study not only proposes a simple and attractive approach toward designing next-generation catalysts of graphene-supported and shaped nanocrystals but also provides an effective method for surface cleaning of organic surfactant-protected nanoparticles.

2. EXPERIMENTAL SECTION

2.1. Chemicals. $[\text{Pd}(\text{acac})_2]$ (99%), $[\text{Pt}(\text{acac})_2]$ (99%), $\text{HAuCl}_4 \cdot 3\text{H}_2\text{O}$, and $[\text{Cu}(\text{acac})_2]$ were purchased from Alfa Aesar. PVP (MW = 30 000, A.R.), $\text{NaI} \cdot 2\text{H}_2\text{O}$ (A.R.), and dimethylformamide (DMF) were purchased from Sinopharm Chemical Reagent Co. Ltd. (Shanghai, China). E-TEK Pt/C (nominally 40% by wt. of 3.2 nm Pt nanoparticles on Vulcan XC-72 carbon support) was purchased from Alfa Aesar. Perchloric acid (HClO_4 , A.R.), acetone, and KOH were obtained from Tianjin Chemical Reagent Co. Ltd. Methanol was obtained from Beijing Chemical Works. The water used in all experiments was supplied by a Water Purifier Nanopure water system ($18.3 \text{ M}\Omega \cdot \text{cm}$). All reagents were used as received without further purification. Moreover, all glassware was washed with Aqua Regia (HCl/HNO_3 with a volume ratio of 3:1) and rinsed with ethanol and ultrapure water. (**Caution!** Aqua Regia is a very corrosive oxidizing agent, which should be handled with great care.)

2.2. Synthesis of Water-Soluble Graphene. Graphene oxide (GO) was synthesized from natural graphite by a modified Hummers method.¹⁶ The graphene sheets were obtained by a simple one-step hydrothermal approach. In a typical synthesis, the as-synthesized GO was first dispersed in DMF (2 mg/mL) under ultrasonic treatment for 30 min, and then PVP (160.0 mg) and NaI solution (2 mL, 0.15 g/mL) were dissolved in 10 mL of GO solution under vigorous stirring. After 30 min of stirring, the resulting homogeneous brown solution was transferred to a Teflon-lined stainless steel autoclave. The sealed vessel was then heated at 150°C for 8 h before it was cooled to room temperature. The resulting black solution was separated and purified with acetone by centrifugation and sonication for three times. The products were finally dispersed in water for further use.

2.3. Synthesis of Pd, Pt, and PtPd Nanocubes Supported on Reduced Graphene Oxide (RGO). For the synthesis of Pd/RGO, Pt/RGO, and PtPd/RGO, respectively, $\text{Pd}(\text{acac})_2$ (50 mg), or $\text{Pt}(\text{acac})_2$ (60 mg), or 25 mg of $\text{Pd}(\text{acac})_2$ and 30 mg of $\text{Pt}(\text{acac})_2$ were mixed with PVP (160 mg), and NaI solution (2 mL, 0.15 g/mL) in 10 mL of DMF solution of graphene oxide. The resulting homogeneous deep brown solution was then treated under the same conditions as those used in the preparation of water-soluble graphene.

2.4. Synthesis of PdCu Alloy Nanocrystals Supported on RGO. $[\text{Pd}(\text{acac})_2]$ (25 mg), $[\text{Cu}(\text{acac})_2]$ (21 mg), PVP (160 mg), and NaI solution (2 mL, 0.15 g/mL) were mixed together in 10 mL of DMF solution of graphene oxide. The resulting homogeneous deep brown solution was then treated under the same conditions as those used in the preparation of water-soluble graphene.

2.5. Synthesis of PdAu Alloy Nanocrystals Supported on RGO. $[\text{Pd}(\text{acac})_2]$ (25 mg), $\text{HAuCl}_4 \cdot 3\text{H}_2\text{O}$ (20 mg), PVP (160 mg), and NaI solution (2 mL, 0.15 g/mL) were mixed

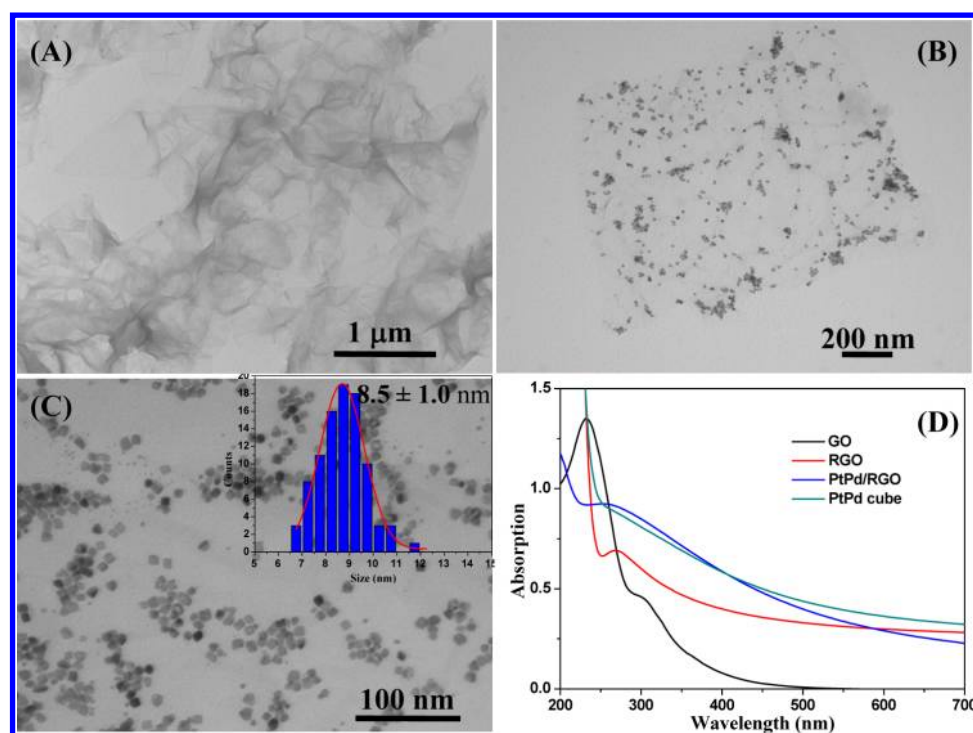


Figure 1. (A) TEM image of reduced graphene oxide (RGO). (B, C) Representative TEM micrographs of PtPd nanocubes supported on RGO (PtPd/RGO) at different magnifications. The inset in (C) shows the particle size distribution histogram. (D) UV-vis spectra of GO, RGO, PtPd/RGO, and the unsupported PtPd alloy nanocubes in water.

together in 10 mL of DMF solution of graphene oxide. The resulting homogeneous deep brown solution was then treated under the same conditions as those used in the preparation of water-soluble graphene.

2.6. Synthesis of Unsupported PtPd Alloy Nanocubes. $[\text{Pd}(\text{acac})_2]$ (25 mg), $[\text{Pt}(\text{acac})_2]$ (30 mg), PVP (160 mg), and a NaI solution (2 mL, 0.15 g/mL) were mixed together in 10 mL of DMF. The resulting homogeneous deep brown solution was then treated under the same conditions as those used in the preparation of water-soluble graphene.

2.7. Material Characterization. UV-vis spectra were recorded on a VARIAN CARY 50 UV/vis spectrophotometer. The size and shape of the products were examined by using a Hitachi H-600 transmission electron microscope (TEM) operated at 100 kV. The samples were prepared by dropping a water dispersion of samples onto carbon-coated copper TEM grids using pipettes and dried under ambient condition. To examine the crystallinity of the products, powder X-ray diffraction (XRD) was performed on a D8 ADVANCE (Germany) using Cu $K\alpha$ radiation with a Ni filter ($\lambda = 0.154059$ nm at 30 kV and 15 mA). High-resolution TEM (HRTEM) images and the corresponding live fast Fourier transform (FFT), high-angle annular dark-field scanning transmission electron microscopy (HAADF-STEM) images, element analysis mapping, and EDX were all carried out on a JEM-2010(HR) microscope operated at 200 kV. The compositions of the products were determined by an inductively coupled plasma-atomic emission spectrometer (ICP-AES, X Series 2, Thermo Scientific USA). X-ray photoelectron spectroscopy (XPS) measurements were performed by using a VG Thermo ESCALAB 250 spectrometer (VG Scientific) operated at 120 W. The binding energy was calibrated against the carbon 1s line. The Fourier-transformed infrared spectroscopy (FTIR) study was conducted with a

VERTEX 70 FTIR (10 mg catalysts, KBr wafer technique). Thermogravimetric analysis (TGA) was performed on a NETZSCH STA 449F3 system equipped with a gas controller and a recirculating stage cooling bath set at 22 °C. A sample of 10 mg of the PtPd/RGO composites was used for analysis. The temperature ranged from 20 to 900 °C in an air atmosphere with a heating rate of 10 °C/min. The final mass remaining after the analysis was used to calculate the total metal loading (wt %).

2.8. Electrochemical Measurements. Before each experiment, a glassy carbon (GC) electrode (3.0 mm in diameter) was first polished with alumina slurries (Al_2O_3 , 0.05 μm) on a polishing cloth to obtain a mirror finish, followed by sonication in 0.1 M HNO_3 , 0.1 M H_2SO_4 , and pure water for 10 min, successively. To prepare a catalyst-coated working electrode, 10 μL of the 2 mg/mL suspension in pure water was drop-coated on the polished electrode surface by a microliter syringe, followed by drying in vacuum at room temperature. Afterward, the catalyst was covered with a thin layer of Nafion (0.1 wt % in water, 5 μL) to ensure that the catalyst was tightly attached to the electrode surface during the electrochemical measurements.

Voltammetric measurements were carried out with a CHI 750D electrochemical workstation. The electrode prepared above was used as the working electrode. A Ag/AgCl (in 3 M NaCl, aq.) combination isolated in a double junction chamber and a Pt coil were used as the reference and counter electrodes, respectively. All electrode potentials in the present study were referred to this Ag/AgCl reference. The working electrodes were first activated with cyclic voltammograms (CVs) (−0.2 to 1.0 V at 100 mV/s) in N_2 -purged 0.1 M HClO_4 solution until a steady CV was obtained. To measure methanol electro-oxidation, the solution of 0.1 M HClO_4 + 1 M CH_3OH was purged with N_2 gas before measurements were taken, and the CVs were recorded in a potential window between −0.2 and

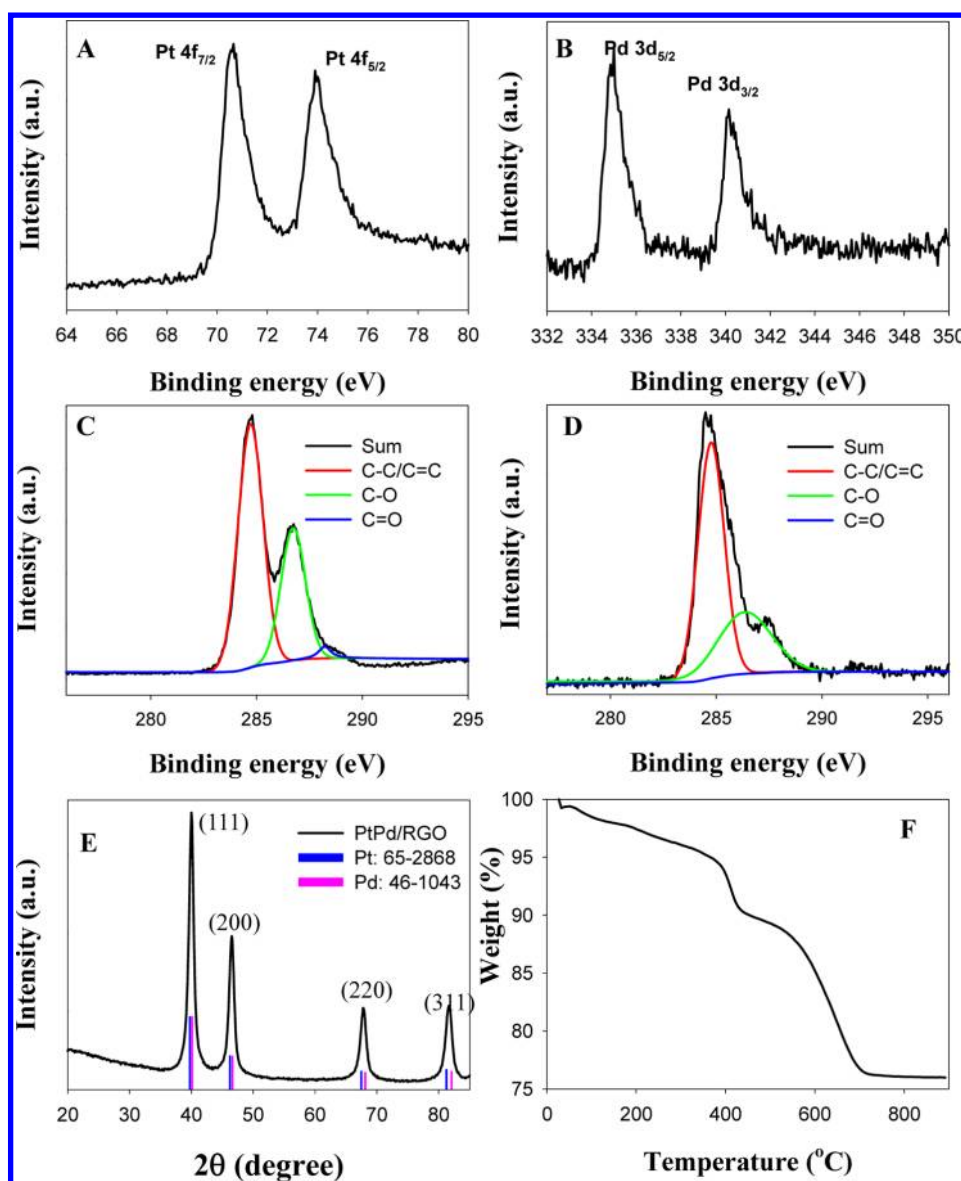


Figure 2. (A, B) XPS of the PtPd/RGO composites: (A) Pt 4f region, (B) Pd 3d region. (C, D) XPS spectra of C 1s of GO (C) and PtPd/RGO (D). (E) XRD pattern of the as-prepared PtPd/RGO composites. For comparison, bulk Pt and Pd from the JCPDS are also presented. (F) Thermogravimetric analysis for the PtPd/RGO measured from 20 to 900 °C in air atmosphere with a heating rate of 10 °C/min.

1.0 V at a scan rate of 50 mV/s in acidic solution. The amperometric current density–time (*i*–*t*) curves were measured at a mixed potential of 0.62 V for 1000 s in 0.1 M HClO₄ + 1.0 M CH₃OH. Electrochemical accelerated durability tests (ADTs) were employed to evaluate the long-term performance of the catalysts. Using the same system as in a CV test, ADT was conducted in the current study with CV curves between –0.2 and 1.0 V in 0.1 M HClO₄ + 1.0 M CH₃OH solutions at a scan rate of 100 mV/s. For each catalyst, the current was normalized to the loading of noble metals (Pt + Pd) to obtain mass activity. All experiments were conducted at room temperature.

2.9. Plasma Cleaning. Plasma cleaning was carried out in a Plasma cleaner (PDC-32G, Harrick Plasma). The catalyst-modified electrodes were cleaned for 15 min under optimal conditions (low level RF and 500 μm vacuum), and then used for cyclic voltammogram measurements.

2.10. CO Stripping. For the CO stripping experiments, CO gas (99.9% purity) was preadsorbed on the electrocatalyst-

modified glassy carbon electrode by bubbling through the electrolytes for 15 min while holding the electrode potential at 0.00 V (vs Ag/AgCl reference electrode) in 0.1 M HClO₄. After N₂ purging for another 15 min to eliminate any dissolved CO in the electrolyte, the adsorbed CO was oxidized by CV with a scan rate of 50 mV/s, and the CO stripping curve was taken. Two subsequent CV cycles were also recorded to verify the complete oxidation of the adsorbed CO.

3. RESULTS AND DISCUSSION

3.1. Synthesis and Characterization of Graphene-Supported PtPd Alloy Nanocubes. In the present study, a facile hydrothermal synthetic strategy was developed to synthesize water-soluble reduced graphene oxide (RGO) and RGO-supported metal nanocrystals. The morphologies of GO, RGO, and PtPd nanocubes deposited on RGO (PtPd/GO) were first characterized by TEM. Figure 1A shows the representative TEM image of RGO dispersed in water. Similar

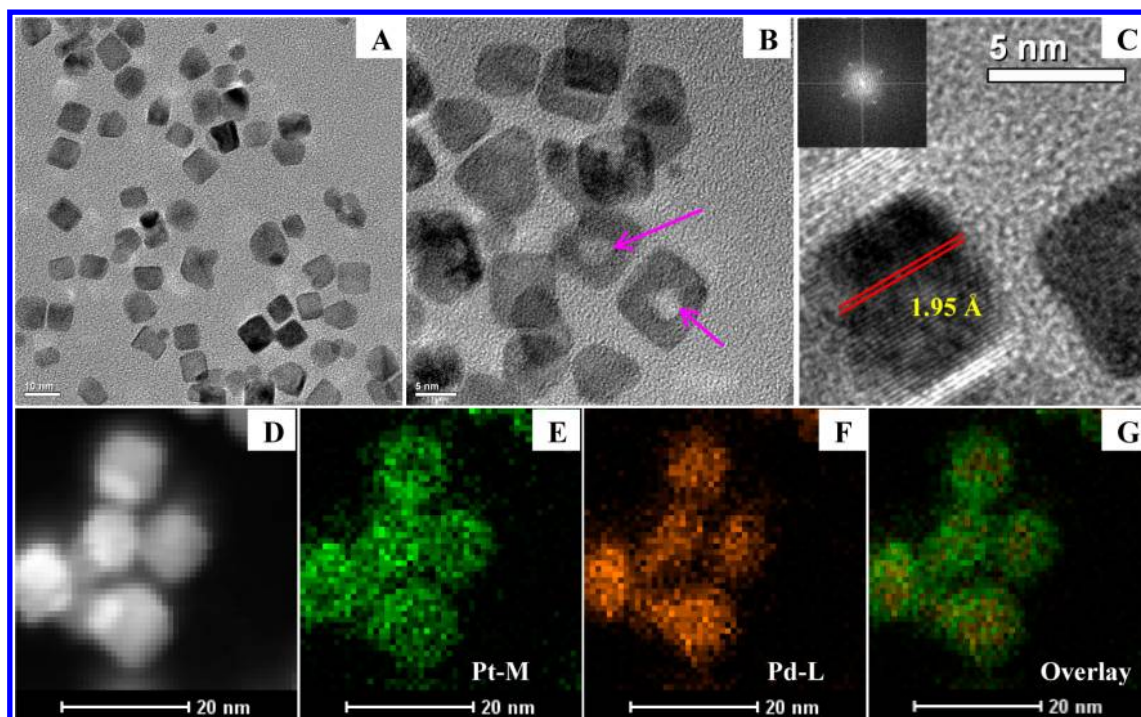


Figure 3. (A–C) High-resolution TEM micrographs of the PtPd alloy nanocubes supported on the RGO surface at different magnifications. The inset in (C) shows the FFT pattern of an individual PtPd nanocrystal. (D) The high-angle annular dark-field (HAADF)-STEM image of PtPd/RGO, and the corresponding elemental mapping of (E) Pt, (F) Pd, and (G) the overlay.

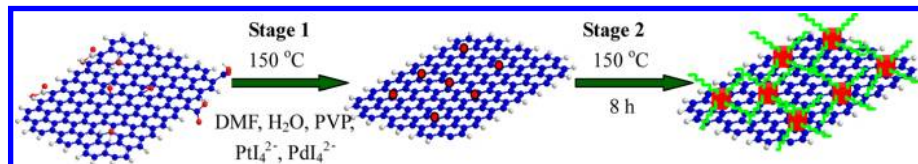
to the morphology of GO shown in Figure S1 (Supporting Information), the obtained RGO nanosheets after the hydrothermal process are well-dispersed without obvious aggregation, indicating an excellent dispersibility of RGO in water. Figure 1B,C shows the TEM images of PtPd/RGO at different magnifications. It can be seen that the prepared nanoparticles are uniformly distributed on the RGO surface. It should be noted that almost no nanoparticles can be observed outside the RGO sheets, indicating that RGO serves here as a template for nanoparticle formation. One hundred fifty nanoparticles were randomly selected to measure the particle size and shape distributions. From the particle size distribution histogram shown in Figure 1C, inset, the as-prepared nanocrystals exhibit an average size of 8.5 ± 1.0 nm with 82% cubes and 18% irregular shapes. To study the effect of RGO on the catalytic activity of PtPd nanocubes, the unsupported PtPd nanocubes were also synthesized according to the procedure described in the Experimental Section. Figure S2 (Supporting Information) displays the TEM micrographs at different magnifications, size distribution histogram, and EDX of the unsupported PtPd nanocubes, from which the average size was calculated to be 8.3 ± 1.0 nm, very close to that of the PtPd nanocubes supported on RGO.

The formation of GO, RGO, and PtPd/RGO as well as the unsupported PtPd nanocubes was also characterized by UV–vis measurements in aqueous solution (Figure 1D). In the absorption spectrum of GO, the absorptions at 232 and 301 nm can be ascribed to the π – π^* transitions of aromatic C=C bonds and the n – π^* transitions of C=O bonds.¹⁷ However, after the hydrothermal treatment with the metal precursors, the absorption peak at 232 nm red shifts to 269 nm and the peak at 301 nm disappears, suggesting the formation of RGO.¹⁸ Note that the UV–vis absorption of the unsupported PtPd alloy nanocubes exhibits a typical Mie exponential decay profile with

no obvious absorption peak, which was usually observed with the small metal nanoparticle solutions.¹⁹ For the PtPd/RGO composites, a broad peak centered at 260 nm appears, indicating the existence of RGO. The formation of RGO and PtPd/RGO hybrid materials can also be reflected from the solution color changes. Figure S3 (Supporting Information) shows the digital photographs of DMF solutions of GO and $\text{Pt}(\text{acac})_2 + \text{Pd}(\text{acac})_2$ and the aqueous solutions of the as-prepared RGO and PtPd/RGO. With the reduction of GO and the metal precursors by hydrothermal reaction, the color of GO changed from yellow to dark and the light red-colored metal precursor solution turned to dark brown, indicating the formation of RGO and PtPd/RGO, respectively. More interestingly, this facile method could also be applied to the synthesis of other monometallic or alloy nanoparticles supported on RGO, such as Pt/RGO, Pd/RGO, PdCu/RGO, PdAu/RGO, and PdAg/RGO. From the TEM images shown in Figure S4 (Supporting Information), the as-synthesized nanocrystals are uniformly distributed on the RGO surface by using the synthetic protocols illustrated in the Experimental Section. Note that the morphology of the RGO-supported nanocrystals could be easily controlled by using the proper surfactants during the hydrothermal process. These results indicate that the procedure introduced here provides a universal method for facile synthesizing graphene-supported (alloy) metal nanocrystals.

The oxidation states of Pt, Pd, and carbon of GO and RGO were investigated by XPS measurements. Figure 2A,B shows the Pt 4f and Pd 3d regions of the PtPd/RGO composites, respectively. The peaks at 70.6 and 74.0 eV in the Pt 4f photoelectron spectrum could be assigned to the binding energies of Pt 4f_{7/2} and Pt 4f_{5/2} of metallic Pt⁰, respectively.^{4c,20} The peaks at 335.0 and 340.2 eV in the Pd XPS spectrum are attributed to the binding energies of Pd 3d_{5/2} and Pd 3d_{3/2},

Scheme 1. Schematic Illustration of the Procedure for One-Pot Hydrothermal Synthesis of RGO-Supported PtPd Alloy Nanocubes. Stage 1: The Reduction of GO and the Nucleation of Nanocrystals. Stage 2: The Growth Process of Alloy Nanocubes



respectively. These binding energies are comparable to those of palladium metal, confirming the zerovalent state of the Pd.^{20b} The deconvoluted C 1s spectra of GO and RGO are shown in Figure 2C,D. The three fitted peaks can be assigned to the binding energies of carbon in C=C/C–C, C–O (epoxy/hydroxyls), and C=O (carbonyl/ketone), respectively.^{18,21} Compared to Figure 2C, the peak intensities of C–O and C=O in the spectrum of RGO (Figure 2D) decreased significantly, indicating that most oxy-functional groups have been removed after the hydrothermal process.¹⁸ XPS data further indicate that Pt and Pd precursors and GO are reduced simultaneously. The XRD pattern of the PtPd/RGO composites (Figure 2E) exhibits the characteristic fcc lattice structure. The clear diffraction peaks with 2θ at 40.0, 46.5, 67.8, and 81.7° could be indexed to the (111), (200), (220), and (311) planes.^{4c} It should be noted that, compared to the JCPDS data of bulk Pt and Pd (blue and pink bars), the diffraction peaks from the PtPd/RGO locate between the positions expected from pure Pt and Pd, strongly indicating the formation of alloyed PtPd nanocrystals. Such a phenomenon has also been observed in other bimetallic alloy nanomaterials.^{4c,22} Moreover, neither a Pt nor a Pd single component peak was observed, confirming the presence of only a single phase of PtPd alloys supported on the RGO surface. The average size of the PtPd nanoparticles can also be calculated based on the broadening of the (200) diffraction peak according to Scherrer's equation: $d = 0.9\lambda/B_{20}\cos\theta$, where λ represents the wavelength of the X-ray, θ is the angle of the peak, and B_{20} is the width of the peak at half height. The average size of PtPd alloy nanoparticles deposited on the RGO was approximately 8.9 nm, which is in good agreement with the TEM data. Meanwhile, the loading of PtPd nanocrystals on the RGO could be easily measured accurately through the thermogravimetric analysis (TGA). From the TGA curve shown in Figure 2F, the loading of the PtPd alloy nanocubes supported on RGO was calculated to be 76 wt %.

HRTEM, HAADF-STEM, and EDX measurements were also carried out to characterize the morphology, crystal structure, and composition of the PtPd nanocubes. The HRTEM images shown in Figure 3A,B at different magnifications show that most of the as-synthesized PtPd nanocrystals exhibit a cubic shape. Interestingly, some of the nanocubes have hollow interiors (indicated by pink arrows in Figure 3B), which can be ascribed to the I[−]-induced galvanic replacement reaction between Pd nanocrystals and the Pt precursors.^{7b} The high-quality single-crystalline nature of the as-prepared PtPd alloy cubes was confirmed by the HRTEM image of a single nanocrystal (Figure 3C). The analysis showed that the lattice fringes with an interplanar distance of 0.195 nm are perpendicular to the edge direction of each nanocube. The spacing of 0.195 nm is between 0.194 and 0.196 nm, corresponding to the interplanar (200) distance of fcc palladium and platinum.^{7b} The corresponding fast Fourier-transform (FFT) pattern (Figure 3C, inset) indicates that the

cubic single crystals consist of (100) surfaces.²³ The element mapping images revealed that both palladium and platinum have a homogeneous distribution in each nanocube (Figure 3D–G), suggesting the formation of an alloy structure. The atomic ratio of Pt/Pd was determined by energy-dispersive X-ray spectroscopy (EDX) and inductively coupled plasma-atomic emission spectrometry (ICP-AES) analysis. From the EDX measurement (Figure S5, Supporting Information), these PtPd nanocubes are essentially alloy particles containing 77 wt % platinum and 23 wt % palladium, which agrees well with the ICP-AES analysis (Pt/Pd = 75:25). Figure S6 (Supporting Information) shows the Raman spectra of GO, RGO, and PtPd/RGO. In the case of GO, a sharp D band at 1360 cm^{−1} and a G band at 1608 cm^{−1} were observed. After the hydrothermal treatment, the ratio of D/G was calculated to be about 0.94, which is higher than that of the initial GO (~0.87), indicating the successful reduction of GO to RGO. At the same time, the appearance of the D and G bands from the PtPd/RGO composites further suggests the deposition of PtPd alloy nanocubes on the RGO support.

It is widely accepted that the formation of nanocrystals (NCs) in a solution system consists of a nucleation stage and a subsequent Ostwald ripening growth on the existing seeds.^{4c,24} The rates of nucleation and subsequent NC growth are the key parameters in the synthesis of shape-controlled NCs. Ideally, a large number of critical nuclei should be formed in a short interval of time, followed by the simultaneous and steady growth of those nuclei. A relatively slow rate in crystal growth usually results in nanocrystals more selectively in crystal directions and benefits the shape control of NCs. In our synthesis, the use of DMF is crucial. As is known to all, DMF has been widely used as a weak reducing agent with the production of CO at its boiling point (153 °C). The endogenous CO could serve as both a reducing agent and an effective protecting agent during the formation of nanoparticles.²⁵ At the same time, PVP could be used as a stabilizer to prevent the aggregation of nanocrystals. In addition, NaI was selected to play a dual-function role in the synthesis: (1) to coordinate with Pd or Pt ions by iodide and thus lower the electrical potentials of Pd or Pt precursors for slow reaction and (2) to selectively adsorb to (100) facets and manipulate the growth of various facets. The standard reduction potential (E^0) of Pt(II)/Pt pairs is typically much more positive than that of Pd(II)/Pd when they are in the same coordination. Previous studies have shown that, when I[−] was introduced into the DMF solutions of [Pt(acac)₂] and [Pd(acac)₂], respectively, the [Pd(acac)₂] solution became much darker immediately, whereas the [Pt(acac)₂] remained almost unchanged until after several hours.^{7b} Therefore, in DMF solution, the reduction of [PdI₄]^{2−} is more favorable than [Pt(acac)₂], which usually results in the formation of hollow PtPd alloy nanocubes. However, in the present study, when GO was added into the mixture, the color of the solution became dark immediately

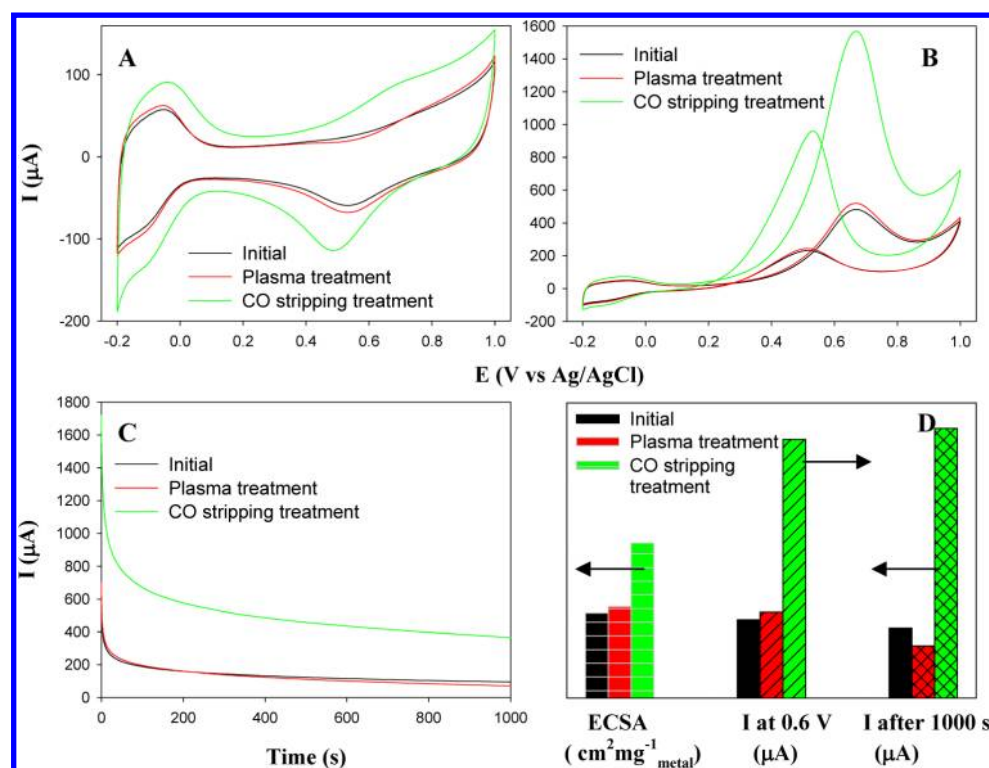


Figure 4. Electrochemical measurements of the PtPd/RGO treated with different methods. Cyclic voltammograms of the PtPd/RGO in 0.1 M HClO₄ (A) and in 0.1 M HClO₄ + 1.0 M CH₃OH solution (B). Potential scan rate of 50 mV/s. (C) Chronoamperometric curves of methanol oxidation at 0.62 V in 0.1 M HClO₄ + 1.0 M CH₃OH solution. (D) The comparison of ECSA and the methanol oxidation currents on the PtPd/RGO catalyst before and after different treatments.

Table 1. Summary of the CO Stripping Effect on the Area of the H_{desorption} Region ($A_{Hdesorption}$), Methanol Oxidation Current at Peak Potentials (I_{max}), and the Current after 1000 s (I_{1000s}) at the Studied Three Electrodes^a

catalysts	$A_{Hdesorption}$ (cm ²)			I_{max} (μA)			I_{1000s} (μA, after 1000 s)		
	before	after	increase	before	after	increase	before	after	increase
PtPd/RGO	1.15	2.10	83%	477	1576.5	230%	94.9	365.3	285%
PtPd cube	0.18	1.70	840%	201.8	1296	542%	18.9	319.6	1591%
Pt/RGO	0.04	0.09	120%	28.2	145.8	428%	2.295	15.96	595%

^aData acquired from CVs and chronoamperometric curves shown in Figure 4 and Figure S7 (Supporting Information).

(Figure S3C, Supporting Information). This suggests that the addition of GO could influence the reaction process, thus resulting in the formation of alloy PtPd nanocubes instead of a hollow structure. In addition, the long stirring time (30 min) before the transfer to the autoclave is also helpful for the formation of [PdL₄]²⁻ and [PtL₄]²⁻ simultaneously. On the basis of the above discussion, we proposed a plausible growth mechanism for the formation of alloyed PtPd nanocubes on the RGO surface, as shown in Scheme 1. In the first stage, GO was reduced to RGO when the temperature was raised to 150 °C, and simultaneously, the early formed metal nuclei attached onto the surface of the RGO sheets because of the strong interaction between them. In the second stage, the nuclei grew gradually into the cubic shape under the protection of PVP.

3.2. Enhanced Electrocatalytic Performance by Effective Particle Surface Cleaning with CO Stripping Treatment. High stability of nanoparticles is usually realized by the surface capped with organic ligands (serve as surfactants), which will largely reduce their catalytic activity when they are used as catalysts. In the past few years, various methods have been applied to clean or remove these surfactants, such as thermal annealing, acetic acid washing,

plasma cleaning, and UV-ozone irradiation. However, these methods require either extremely high temperature or long treatment time. At the same time, the cleaning process may cause the change in particle size and morphology, especially for the shaped nanocrystals. Therefore, it is essential to develop a simple and effective strategy to clean the surface of nanoparticles and make them catalytically active. Here, we demonstrate that CO stripping is an efficient method to clean the particle surface and thus improve the electrocatalytic activity of the PVP- and I⁻-stabilized PtPd nanocrystals. Figure 4 shows the CVs of the PtPd/RGO supported on a glassy carbon electrode before and after CO stripping and plasma treatments. Compared to the untreated (initial) electrode, the CO stripping-treated electrode exhibited an increased electrochemically active surface area (ECSA), enhanced catalytic activity toward methanol oxidation, and improved stability. From the comparison shown in Figure 4D, after the CO stripping, the ECSA, methanol oxidation current at 0.6 V, and the stability of the PtPd/RGO composites increased by 83, 230, and 285%, respectively. In contrast, the commonly used plasma cleaning method has nearly no obvious enhancement for the electrochemical activity and stability of PtPd/RGO.

To demonstrate the universality of the CO stripping for the surface cleaning of the PVP- and Γ^- -stabilized nanoparticles, control experiments were also performed on the Pt/RGO and unsupported PtPd alloy nanocubes (Figure S7, Supporting Information). It can be seen clearly that, similar to the PtPd/RGO, the ECSA, methanol oxidation current, and the stability from both of the Pt/RGO and the unsupported PtPd alloy nanocubes are enhanced significantly after the CO stripping treatment. By CO stripping, the improvement percentages of the area of the $H_{\text{desorption}}$ region ($A_{H_{\text{desorption}}}$), methanol oxidation currents at peak potentials (I_{max}), and the currents after 1000 s ($I_{1000\text{s}}$) at the studied three electrodes are summarized in Table 1.

In contrast, as seen from Figure S8 (Supporting Information), the CVs of surfactant-free commercial Pt/C catalysts showed almost no change after the CO stripping treatment, except for some decrease of the methanol oxidation current, which is similar to the previous studies.²⁶ It was found that the CO annealing could result in a decreased fraction of high-index surface facets of Pt nanoparticles and thus lower their electrocatalytic activities. These results indicate clearly that the CO stripping process can be used as an efficient surface cleaning method for the application of organic layers protected nanomaterials in catalysis. Interestingly, recent studies also showed that the CO-annealing process can be used to induce the surface segregation for alloy Pt_3Co nanoparticles on the basis of the different adsorption enthalpies of Pt and Co.²⁷ It was found that CO annealing induced a similar effect as thermal annealing to form a Pt shell around an alloy core without any leaching of Co into the electrolyte. Moreover, CO annealing is better suited for nanocrystals, since the particle size remains unaltered and no active surface area loss occurs. As a consequence, Pt enrichment at the surface of nanocrystals can enhance their electrocatalytic activity.

To ascertain the surface cleaning and activity enhancement mechanism of CO stripping treatment, FTIR spectra were collected from PtPd/RGO before and after the CO stripping (Figure 5). Note that the catalysts were removed from the GC surface after the CO stripping test to make a pellet for FTIR measurements. In comparison, the FTIR spectrum of pure PVP molecules was also obtained. For the pure PVP molecule, the characteristic band at 734 cm^{-1} is due to the plane bending

vibration of long-chain $-(\text{CH}-\text{CH}_2)_n-$. The bands at 1071 and 1666 cm^{-1} could be attributed to the C–N symmetric stretching and the $\text{C}=\text{O}$ stretching vibration, respectively. The bands between 1400 and 1500 cm^{-1} are due to the absorption peaks of $-\text{N}-\text{C}-$. The band at 2882 cm^{-1} is due to the symmetric stretching vibrations of $-\text{CH}_2-$, whereas the band at 2952 cm^{-1} is attributed to the asymmetric stretching vibration of $-\text{CH}_2-$. The broad absorption bands between 3200 and 3600 cm^{-1} is due to the stretching vibration of adsorbed water.²⁸ In the spectrum of PVP-capped PtPd/RGO composites, almost all the characteristic bands match well to PVP except for the symmetric stretching vibration for C–N shifted from 1071 to 1096 cm^{-1} and $\text{C}=\text{O}$ stretching vibration shifted from 1666 to 1640 cm^{-1} . These results clearly indicate that either N or O atoms of PVP molecules interacted with the PtPd alloy nanocubes by chemisorptions on the surfaces of the nanocubes.^{28a,29} However, after the CO stripping treatment, almost all the characteristics of PVP molecules disappeared, indicating the successful removal of the PVP molecules by CO stripping. Furthermore, we also carried out the CO stripping treatments on the PVP-stabilized Pd-based nanocrystals, such as PdAu and PdAg. Unfortunately, there was no significant change before and after CO stripping tests. Thus, the enhancement effect of the CO stripping might be attributed to the exposure of the active sites after CO stripping and could be only applied to the Pt-based nanocrystals. The strong interaction between Pt and CO molecules could replace the chemisorbed PVP molecules during the preadsorption of the CO. Finally, more surface atoms were exposed and became electrochemically active after CO stripping. The present result is similar to that of another recent study where the surfactant-free Ag nanorods exhibited much enhanced electrocatalytic activity compared with the PVP-stabilized ones.³⁰

3.3. Improved Electrocatalytic Performance of PtPd/RGO for Methanol Oxidation. The electrocatalytic activity of the as-prepared PtPd/RGO composites for methanol oxidation was studied by electrochemical cyclic voltammetry. For comparison, unsupported PtPd alloy nanocubes with the same size and the commercial Pt/C (40 wt %) were also examined. Before the electrochemical measurements, all the glassy carbon (GC)-supported catalysts were subjected to argon plasma treatment, electrochemical polishing between -0.2 and 1.0 V , and CO stripping to obtain surface clean electrocatalysts. Figure 6A shows the typical CVs of the PtPd/RGO, unsupported PtPd alloy nanocubes, and the commercial Pt/C catalysts recorded in N_2 -purged 0.1 M HClO_4 solutions at a potential scan rate of 50 mV/s . Note that the currents have been normalized to the mass of noble metals (Pt and Pd). All the CV curves exhibited three traditional distinctive potential regions associated with H_{upd} adsorption/desorption processes ($\text{H}^+ + \text{e} = \text{H}_{\text{upd}}$) between -0.18 and 0.20 V , the double-layer region from 0.20 to 0.40 V , and the formation of an OH_{ad} layer ($2\text{H}_2\text{O} = \text{OH}_{\text{ad}} + \text{H}_3\text{O}^+ + \text{e}$) beyond 0.4 V . One can see that the double-layer capacitance of the PtPd/RGO composites is much larger than those of unsupported PtPd nanocubes and the commercial Pt/C catalysts, indicating the large surface area of graphene nanosheets,³¹ which renders them the suitable support for the good dispersion of nanoparticle catalysts.

The electrochemically active surface area (ECSA) was calculated by measuring the charge collected in the H_{upd} adsorption/desorption region after double-layer correction

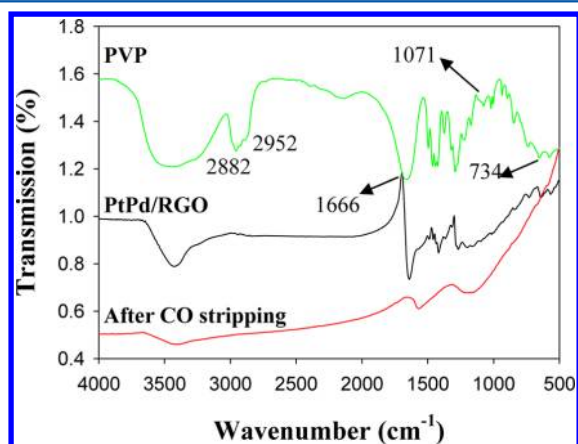


Figure 5. FTIR spectra of PVP-capped PtPd alloy nanocubes supported on the RGO surface before and after the CO stripping treatment. For comparison, the FTIR spectrum of pure PVP molecules is also shown.

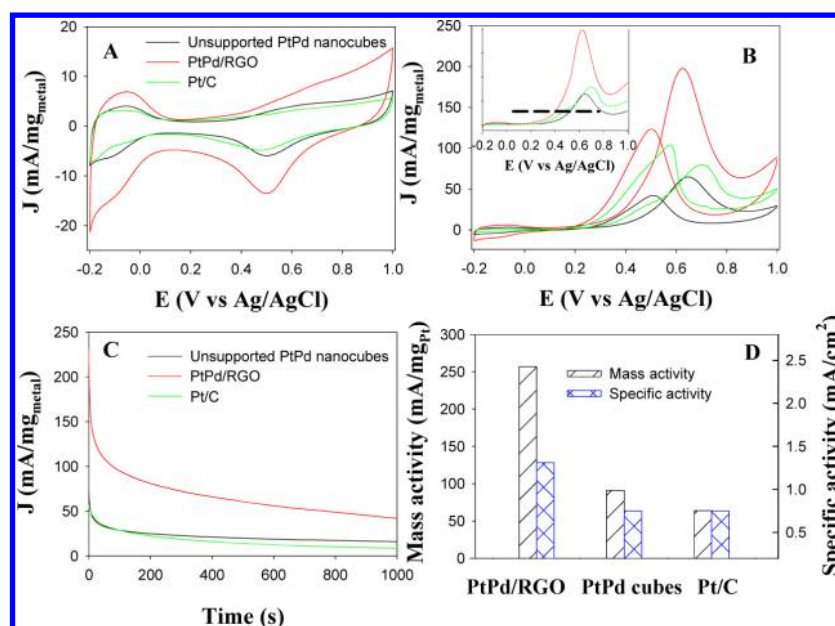


Figure 6. Cyclic voltammograms (CVs) of the unsupported PtPd alloy nanocubes, PtPd/RGO, and the commercial Pt/C catalyst in (A) 0.1 M HClO₄ solution and (B) 0.1 M HClO₄ + 1.0 M CH₃OH solution. (C) Chronoamperometric curves of methanol oxidation at 0.62 V in 0.1 M HClO₄ + 1.0 M CH₃OH solution after the CO stripping treatment. Potential scan rate of 50 mV/s. All currents were normalized to the total mass of noble metals (Pt and Pd). (D) Comparison of mass and specific activities of the three catalysts for methanol oxidation.

and assuming a value of 0.21 mC/cm² for the adsorption of a hydrogen monolayer^{4c,11c,14c,32}

$$\text{ECSA} = Q_{\text{H}} / [\text{metal}] * 0.21 \quad (1)$$

where [metal] represents the loading of Pt and Pd. The ECSAs of the Pt/C, unsupported PtPd alloy nanocube, and PtPd/RGO were calculated to be 85.6, 121.4, and 197 cm²/mg_{metal}, respectively. As observed from other studies, the remarkably increased ECSA with RGO as the support might be attributed to the good dispersion of PtPd alloy nanocubes on the RGO surface (Figures 1 and 3), even though the size of the PtPd nanocubes is larger than that of the Pt nanoparticle in commercial Pt/C.

Figure 6B shows the CVs of methanol oxidation on the three electrodes in 0.1 M HClO₄ + 1.0 M CH₃OH at a scan rate of 50 mV/s. At potentials below 0.40 V, the oxidation current is negligible in all voltammograms because the surface active sites are poisoned by CO_{ads}, an intermediate from dehydrogenation of methanol. With the potential increasing, the oxidation current takes off rapidly, signifying that significant methanol oxidation occurs. Onset potential and current density are the two major parameters to evaluate the catalytic activity of electrocatalysts. From Figure 6B and the inset, the PtPd/RGO composites exhibit a much more negative onset potential of methanol oxidation than the unsupported PtPd alloy nanocubes and the commercial Pt/C catalyst. The oxidation peak potential at PtPd/RGO is 0.62 V, about 30 and 80 mV more negative than those at the unsupported PtPd nanocubes (0.65 V) and the commercial Pt/C (0.70 V). Moreover, at a given oxidation current density (as indicated by the dashed line in Figure 6B, inset), the corresponding potential of methanol oxidation on the PtPd/RGO composites is obviously lower than those on the other two catalysts, further indicating the easier methanol oxidation reaction on the PtPd/RGO. As for the current density of methanol oxidation, the mass-specific activity of PtPd/RGO (198 mA/mg_{Metal}) at 0.62 V is nearly

3.14 times higher than those of the unsupported PtPd nanocubes (63 mA/mg_{Metal}) and commercial Pt/C catalyst (64 mA/mg_{Metal}). The CVs normalized to ECSA were also plotted in Figure S9 (Supporting Information), from which the specific activities of the three catalysts can be calculated. Figure 6D compares the mass and specific activities of the catalysts. It can be seen that the area-specific activity of PtPd/RGO is 1.31 mA/cm², which is 1.75 times higher than those of the unsupported PtPd nanocubes (0.75 mA/cm²) and the commercial Pt/C catalyst (0.75 mA/cm²).

On the other hand, it is generally accepted that, during methanol oxidation at Pt-based catalysts, some poisonous intermediates, such as CHO_{ads} and CO_{ads}, can be strongly adsorbed on the platinum surface, leading to the self-poisoning of catalysts. The ratio of the peak currents associated with the anodic peak in forward (*I_f*) and reverse (*I_r*) is generally used to evaluate the catalyst tolerance to CO poisoning. A higher *I_f*/*I_r* suggests the better electrocatalytic activity and higher CO tolerance.^{2c,33} From Figure 6B, the *I_f*/*I_r* ratio on PtPd/RGO is 1.61, which is much larger than those of the commercial Pt/C catalyst (0.76) and the unsupported PtPd nanocubes (1.52), suggesting enhanced CO tolerance of PtPd/RGO as compared to the other two catalysts.

The long-term stability is one of the most important issues for the application of catalysts in fuel cells. To evaluate the electrochemical stabilities of the catalysts, chronoamperometric (CA) measurements were performed at 0.62 V in 0.1 M HClO₄ + 1.0 M CH₃OH solution (Figure 6C). Apparently, an initial rapid current decay can be observed, probably due to the formation of some intermediate species (CO_{ads} and CHO_{ads}) during the methanol oxidation reaction. After a long period of operation (1000 s), although the current continues to decay gradually, the PtPd/RGO electrocatalyst shows a much lower deterioration rate and higher oxidation current compared to the other two catalysts, demonstrating the prominent electrocatalytic stability of the PtPd/RGO catalysts. To further

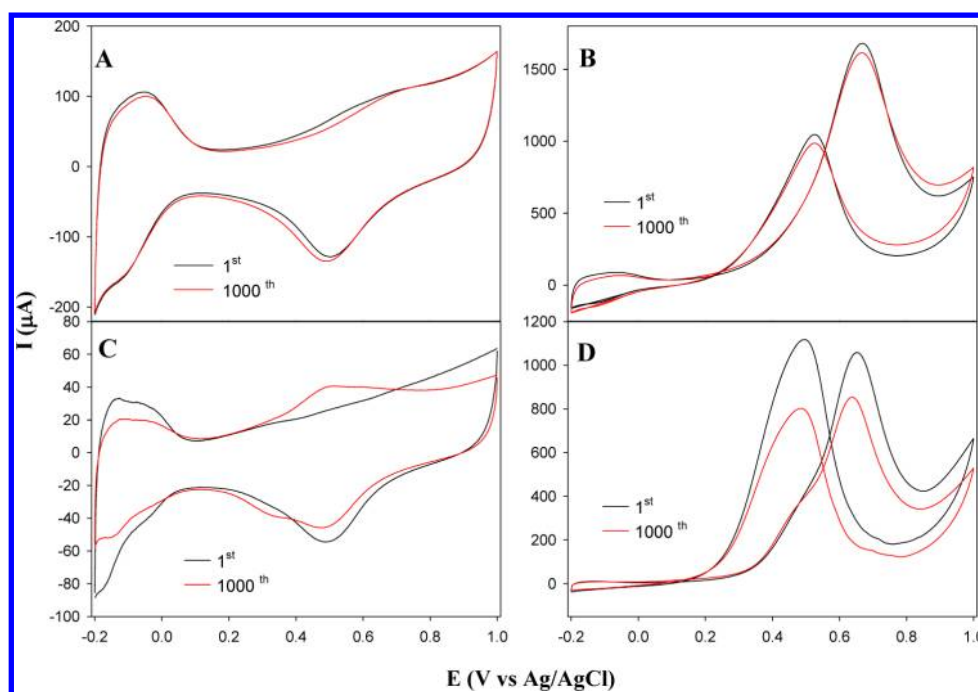


Figure 7. The 1st and the 1000th cyclic voltammetry curves obtained on PtPd/RGO (A, B) and the commercial Pt/C catalyst (C, D) in 0.1 M HClO_4 (left panels) and in 0.1 M HClO_4 + 1.0 M CH_3OH solution (right panels). Potential scan rate of 50 mV/s.

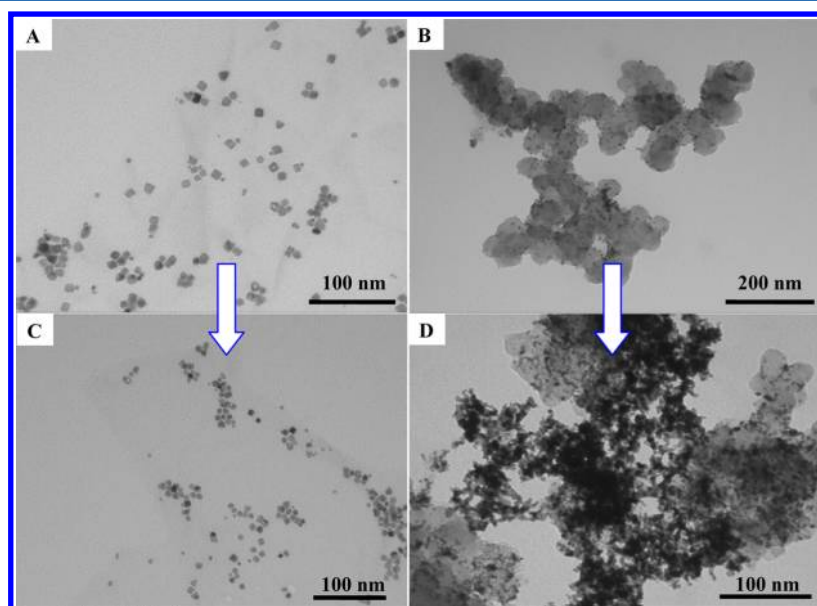


Figure 8. Representative TEM images of PtPd/RGO (A, C) and the commercial Pt/C catalyst (B, D), before (upper panels) and after (lower panels) 1000 accelerated CV test cycles in 0.1 M HClO_4 + 1.0 M CH_3OH solution with a potential scan rate of 50 mV/s.

examine the stability of the PtPd/RGO, accelerated durability tests (ADTs) were also performed, which were carried out in 0.1 M HClO_4 + 1.0 M methanol solution by applying a cyclic potential sweep between -0.2 and 1.0 V at a scan rate of 100 mV/s. The durability was tested by comparing the ECSA and peak currents before and after an accelerated methanol oxidation reaction. As shown in Figure 7, the PtPd/RGO experienced a loss of only 5.6% and 4.1%, respectively, of the initial ECSA and peak current after 1000 cycles of methanol oxidation. However, the commercial Pt/C catalyst lost 25.7% and 20.6% of the ECSA and the initial peak current after 1000 cycles of methanol oxidation reaction. Such results again

indicate that the PtPd/RGO exhibits enhanced durability toward methanol oxidation.

The loss of the ECSA due to the corrosion of the catalyst support and the subsequent agglomeration of Pt nanoparticles have been recognized as the main reasons for the rapid decrease of the catalytic activity and durability of electrocatalysts. Thus, to understand the different durability of the PtPd/RGO and Pt/C, the catalysts were collected by sonicating the glassy carbon electrodes in water after the durability tests (1000 cycles), and their structures were characterized by TEM measurements. As shown in Figure 8, the Pt nanoparticle size of the commercial Pt/C catalyst increases from 2–5 nm to 5–

10 nm upon the durability test, indicating substantial growth or aggregation of Pt nanoparticles due to the Ostwald ripening. In contrast, no significant changes in morphology, particle size, and size distribution were observed in the case of the PtPd/RGO catalyst after 1000 cycles. These results provided direct evidence that the commercial Pt/C catalyst suffers heavily from the Pt particle aggregation, resulting in the degradation of catalytic performance. On the contrary, the PtPd/RGO can keep its morphology very well after electrochemical operation. For the PtPd/RGO, the strong interaction between RGO and the PtPd nanocubes can prevent effectively the ripening process and aggregation of nanocubes during the electrochemical scanning, thereby increasing its long-term durability. Overall, in comparison with the unsupported PtPd nanocrystals, the enhanced electrocatalytic performance of RGO-supported PtPd nanocubes could be partially ascribed to the improved stability and their high dispersion on the RGO surface.

3.4. CO Stripping. CO has been identified as a major poison species for Pt catalysts in the process of alcohol oxidation. Thus, CO stripping could serve as a model probe to evaluate the CO tolerance of catalysts.³⁴ Figure 9 summarizes the CO stripping experiments on the three studied catalysts in 0.1 M HClO₄ solution. On the three electrodes, the hydrogen desorption peaks were fully suppressed in the first positive-going scan due to the active surface sites blocked by the preadsorbed CO. A broad current peak resulting from the CO oxidation appeared in the potential range from 0.2 to 0.8 V. With the oxidation removal of adsorbed CO, the hydrogen adsorption/desorption peaks recovered in the following scans. Importantly, it can be seen that the onset potential of CO oxidation on PtPd/RGO was observed at 0.225 V, which is much more negative than those of the commercial Pt/C catalysts (0.250 V) and the unsupported PtPd nanocubes (0.423 V). This result indicates that the as-prepared PtPd/RGO composites are active for CO oxidation and exhibit excellent CO tolerance, agreeing well with the above results of methanol oxidation.

4. CONCLUSION

In summary, we have demonstrated here a facile and general approach that could allow the one-pot fabrication of water-soluble and uniform single-crystalline PtPd alloy nanocubes supported on the reduced graphene oxide nanosheets (PtPd/RGO). This method could also be used to synthesize other water-soluble Pt- or Pd-based alloy nanocrystals with the desirable morphology supported on RGO. At the same time, we found that CO stripping treatment could be used as a facile method to remove the chemisorbed PVP molecules and thus activate the catalyst surface. With the clean surface treated by CO stripping, the PtPd/RGO composites exhibited excellent electrocatalytic performance for methanol oxidation with a larger current density and a lower onset potential compared to the commercial Pt/C catalyst and the unsupported PtPd nanocubes. Moreover, the as-prepared PtPd/RGO showed high durability with a loss of only 5.6% and 4.1% of the initial ECSA and peak current after 1000 cycles of methanol oxidation. In sharp contrast, the unsupported PtPd alloy nanocubes and the commercial Pt/C catalyst lost 8.5% and 25.7% of their ECSA and 6.2% and 20.6% of their initial peak currents after 1000 cycles of methanol oxidation reaction. The present work not only provides a facile method to synthesize graphene-supported alloy nanocrystals with special facets but also finds a new method for particle surface cleaning. Moreover, the present

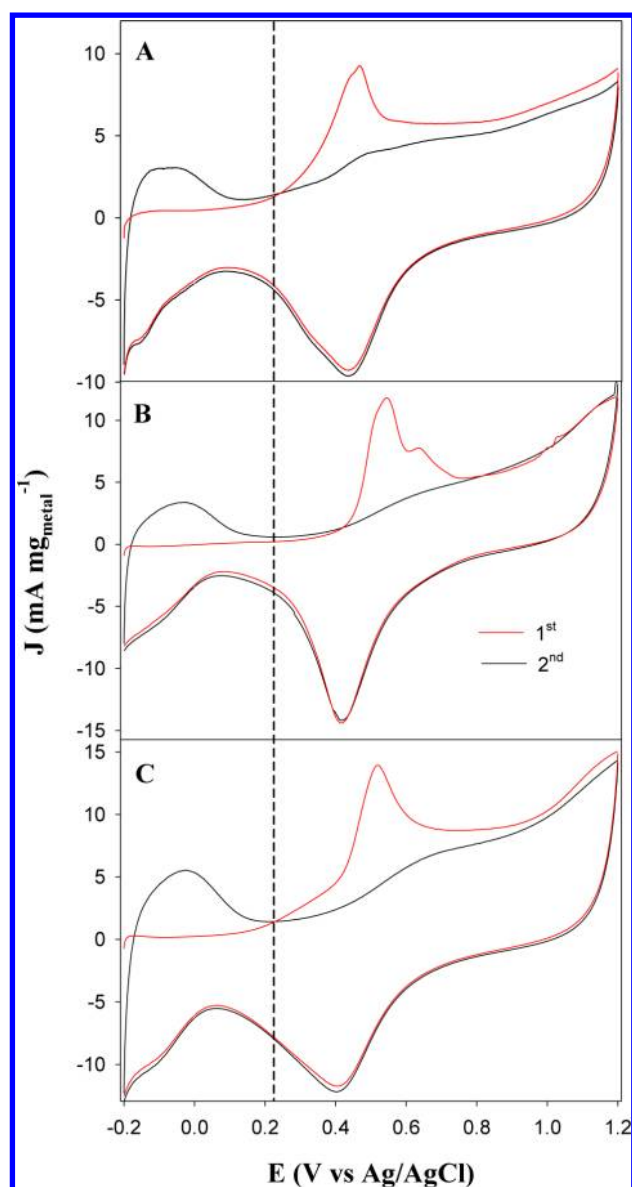


Figure 9. The first (red lines) and the second (black lines) cyclic voltammograms of the commercial Pt/C catalyst (A), unsupported PtPd alloy nanocubes (B), and the PtPd/RGO (C) initially covered with a saturated CO adlayer in CO-free 0.1 M HClO₄. Potential scan rate of 50 mV/s.

work demonstrates that graphene nanosheets are indeed excellent catalyst supports for enhancing the catalytic performance and improving the stability of catalysts.

■ ASSOCIATED CONTENT

Supporting Information

Additional characterizations and more electrochemical measurements of the as-prepared materials. This material is available free of charge via the Internet at <http://pubs.acs.org>.

■ AUTHOR INFORMATION

Corresponding Author

*E-mail: weichen@ciac.jl.cn.

Notes

The authors declare no competing financial interest.

■ ACKNOWLEDGMENTS

This work was supported by the National Natural Science Foundation of China (No. 21275136) and the Natural Science Foundation of Jilin province, China (No. 201215090).

■ REFERENCES

- (1) (a) Yajima, T.; Uchida, H.; Watanabe, M. In-situ ATR-FTIR spectroscopic study of electro-oxidation of methanol and adsorbed CO at Pt–Ru alloy. *J. Phys. Chem. B* **2004**, *108* (8), 2654–2659. (b) Steele, B. C. H.; Heinzel, A. Materials for fuel-cell technologies. *Nature* **2001**, *414* (6861), 345–352. (c) Russell, A. E.; Rose, A. X-ray absorption spectroscopy of low temperature fuel cell catalysts. *Chem. Rev.* **2004**, *104* (10), 4613–4635. (d) Acres, G. J. K. Recent advances in fuel cell technology and its applications. *J. Power Sources* **2001**, *100* (1–2), 60–66.
- (2) (a) Tian, N.; Zhou, Z. Y.; Sun, S. G.; Ding, Y.; Wang, Z. L. Synthesis of tetrahexahedral platinum nanocrystals with high-index facets and high electro-oxidation activity. *Science* **2007**, *316* (5825), 732–735. (b) Chen, W.; Kim, J.; Sun, S. H.; Chen, S. W. Electro-oxidation of formic acid catalyzed by FePt nanoparticles. *Phys. Chem. Chem. Phys.* **2006**, *8* (23), 2779–2786. (c) Chen, W.; Kim, J. M.; Sun, S. H.; Chen, S. W. Composition effects of FePt alloy nanoparticles on the electro-oxidation of formic acid. *Langmuir* **2007**, *23* (22), 11303–11310. (d) Yang, H. Z.; Zhang, J.; Sun, K.; Zou, S. Z.; Fang, J. Y. Enhancing by weakening: Electrooxidation of methanol on Pt₃Co and Pt nanocubes. *Angew. Chem., Int. Ed.* **2010**, *49* (38), 6848–6851.
- (3) (a) Tripkovic, A. V.; Popovic, K. D.; Grgur, B. N.; Blizanac, B.; Ross, P. N.; Markovic, N. M. Methanol electrooxidation on supported Pt and PtRu catalysts in acid and alkaline solutions. *Electrochim. Acta* **2002**, *47* (22–23), 3707–3714. (b) Chen, Y. X.; Miki, A.; Ye, S.; Sakai, H.; Osawa, M. Formate, an active intermediate for direct oxidation of methanol on Pt electrode. *J. Am. Chem. Soc.* **2003**, *125* (13), 3680–3681.
- (4) (a) Chen, A. C.; Holt-Hindle, P. Platinum-based nanostructured materials: Synthesis, properties, and applications. *Chem. Rev.* **2010**, *110* (6), 3767–3804. (b) Lu, Y. C.; Xu, Z. C.; Gasteiger, H. A.; Chen, S.; Hamad-Schifferli, K.; Shao-Horn, Y. Platinum–gold nanoparticles: A highly active bifunctional electrocatalyst for rechargeable lithium–air batteries. *J. Am. Chem. Soc.* **2010**, *132* (35), 12170–12171. (c) Lu, Y. Z.; Chen, W. One-pot synthesis of heterostructured Pt–Ru nanocrystals for catalytic formic acid oxidation. *Chem. Commun.* **2011**, *47* (9), 2541–2543. (d) Greeley, J.; Stephens, I. E. L.; Bondarenko, A. S.; Johansson, T. P.; Hansen, H. A.; Jaramillo, T. F.; Rossmeisl, J.; Chorkendorff, I.; Nørskov, J. K. Alloys of platinum and early transition metals as oxygen reduction electrocatalysts. *Nat. Chem.* **2009**, *1* (7), 552–556.
- (5) (a) Habas, S. E.; Lee, H.; Radmilovic, V.; Somorjai, G. A.; Yang, P. Shaping binary metal nanocrystals through epitaxial seeded growth. *Nat. Mater.* **2007**, *6* (9), 692–697. (b) Chen, W.; Chen, S. W. Oxygen electroreduction catalyzed by gold nanoclusters: Strong core size effects. *Angew. Chem., Int. Ed.* **2009**, *48* (24), 4386–4389.
- (6) (a) Lim, B.; Jiang, M. J.; Camargo, P. H. C.; Cho, E. C.; Tao, J.; Lu, X. M.; Zhu, Y. M.; Xia, Y. A. Pd–Pt bimetallic nanodendrites with high activity for oxygen reduction. *Science* **2009**, *324* (5932), 1302–1305. (b) Yuan, Q.; Zhuang, J.; Wang, X. Single-phase aqueous approach toward Pd sub-10 nm nanocubes and Pd–Pt heterostructured ultrathin nanowires. *Chem. Commun.* **2009**, No. 43, 6613–6615. (c) Lee, H. J.; Habas, S. E.; Somorjai, G. A.; Yang, P. D. Localized Pd overgrowth on cubic Pt nanocrystals for enhanced electrocatalytic oxidation of formic acid. *J. Am. Chem. Soc.* **2008**, *130* (16), 5406–5407.
- (7) (a) Wang, L.; Nemoto, Y.; Yamauchi, Y. Direct synthesis of spatially-controlled Pt-on-Pd bimetallic nanodendrites with superior electrocatalytic activity. *J. Am. Chem. Soc.* **2011**, *133* (25), 9674–9677. (b) Huang, X. Q.; Zhang, H. H.; Guo, C. Y.; Zhou, Z. Y.; Zheng, N. F. Simplifying the creation of hollow metallic nanostructures: One-pot synthesis of hollow palladium/platinum single-crystalline nanocubes. *Angew. Chem., Int. Ed.* **2009**, *48* (26), 4808–4812. (c) Peng, Z. M.; Yang, H. Synthesis and oxygen reduction electrocatalytic property of Pt-on-Pd bimetallic heteronanostructures. *J. Am. Chem. Soc.* **2009**, *131* (22), 7542–7543. (d) Lim, B.; Wang, J. G.; Camargo, P. H. C.; Jiang, M. J.; Kim, M. J.; Xia, Y. N. Facile synthesis of bimetallic nanoplates consisting of Pd cores and Pt shells through seeded epitaxial growth. *Nano Lett.* **2008**, *8* (8), 2535–2540. (e) Yin, A. X.; Min, X. Q.; Zhang, Y. W.; Yan, C. H. Shape-selective synthesis and facet-dependent enhanced electrocatalytic activity and durability of monodisperse sub-10 nm Pt–Pd tetrahedrons and cubes. *J. Am. Chem. Soc.* **2011**, *133* (11), 3816–3819.
- (8) (a) Wang, Y. J.; Wilkinson, D. P.; Zhang, J. J. Noncarbon support materials for polymer electrolyte membrane fuel cell electrocatalysts. *Chem. Rev.* **2011**, *111* (12), 7625–7651. (b) Shao, Y. Y.; Yin, G. P.; Gao, Y. Z. Understanding and approaches for the durability issues of Pt-based catalysts for PEM fuel cell. *J. Power Sources* **2007**, *171* (2), 558–566. (c) Ferreira, P. J.; la O', G. J.; Shao-Horn, Y.; Morgan, D.; Makharia, R.; Kocha, S.; Gasteiger, H. A. Instability of Pt/C electrocatalysts in proton exchange membrane fuel cells: A mechanistic investigation. *J. Electrochem. Soc.* **2005**, *152* (11), A2256–A2271.
- (9) (a) Wan, X. J.; Huang, Y.; Chen, Y. S. Focusing on energy and optoelectronic applications: A journey for graphene and graphene oxide at large scale. *Acc. Chem. Res.* **2012**, *45* (4), 598–607. (b) Huang, X.; Qi, X. Y.; Boey, F.; Zhang, H. Graphene-based composites. *Chem. Soc. Rev.* **2012**, *41* (2), 666–686. (c) Guo, S. J.; Dong, S. J. Graphene nanosheet: Synthesis, molecular engineering, thin film, hybrids, and energy and analytical applications. *Chem. Soc. Rev.* **2011**, *40* (5), 2644–2672.
- (10) (a) He, D. P.; Cheng, K.; Li, H. G.; Peng, T.; Xu, F.; Mu, S. C.; Pan, M. Highly active platinum nanoparticles on graphene nanosheets with a significant improvement in stability and CO tolerance. *Langmuir* **2012**, *28* (8), 3979–3986. (b) Wang, X.; Li, X. Y.; Liu, D. P.; Song, S. Y.; Zhang, H. J. Green synthesis of Pt/CeO₂/graphene hybrid nanomaterials with remarkably enhanced electrocatalytic properties. *Chem. Commun.* **2012**, *48* (23), 2885–2887. (c) Maiyalagan, T.; Dong, X. C.; Chen, P.; Wang, X. Electrodeposited Pt on three-dimensional interconnected graphene as a free-standing electrode for fuel cell application. *J. Mater. Chem.* **2012**, *22* (12), 5286–5290. (d) Kamat, P. V. Graphene-based nanoarchitectures. Anchoring semiconductor and metal nanoparticles on a two-dimensional carbon support. *J. Phys. Chem. Lett.* **2010**, *1* (2), 520–527. (e) Kou, R.; Shao, Y. Y.; Mei, D. H.; Nie, Z. M.; Wang, D. H.; Wang, C. M.; Viswanathan, V. V.; Park, S.; Aksay, I. A.; Lin, Y. H.; Wang, Y.; Liu, J. Stabilization of electrocatalytic metal nanoparticles at metal–metal oxide–graphene triple junction points. *J. Am. Chem. Soc.* **2011**, *133* (8), 2541–2547. (f) Singh, R. N.; Awasthi, R. Graphene support for enhanced electrocatalytic activity of Pd for alcohol oxidation. *Catal. Sci. Technol.* **2011**, *1* (5), 778–783.
- (11) (a) Lu, Y. Z.; Chen, W. PdAg alloy nanowires: Facile one-step synthesis and high electrocatalytic activity for formic acid oxidation. *ACS Catal.* **2012**, *2* (1), 84–90. (b) Lu, Y. Z.; Chen, W. Nanoneedle-covered Pd–Ag nanotubes: High electrocatalytic activity for formic acid oxidation. *J. Phys. Chem. C* **2010**, *114* (49), 21190–21200. (c) Chen, X. M.; Wu, G. H.; Chen, J. M.; Chen, X.; Xie, Z. X.; Wang, X. R. Synthesis of “clean” and well-dispersive Pd nanoparticles with excellent electrocatalytic property on graphene oxide. *J. Am. Chem. Soc.* **2011**, *133* (11), 3693–3695. (d) Bianchini, C.; Shen, P. K. Palladium-based electrocatalysts for alcohol oxidation in half cells and in direct alcohol fuel cells. *Chem. Rev.* **2009**, *109* (9), 4183–4206.
- (12) (a) Khomyakov, P. A.; Giovannetti, G.; Rusu, P. C.; Brocks, G.; van den Brink, J.; Kelly, P. J. First-principles study of the interaction and charge transfer between graphene and metals. *Phys. Rev. B* **2009**, *79* (19), 195425. (b) Wang, Q. J.; Che, J. G. Origins of distinctly different behaviors of Pd and Pt contacts on graphene. *Phys. Rev. Lett.* **2009**, *103* (6), 066802.
- (13) Liu, Z. F.; Shamsuzzoha, M.; Ada, E. T.; Reichert, W. M.; Nikles, D. E. Synthesis and activation of Pt nanoparticles with controlled size for fuel cell electrocatalysts. *J. Power Sources* **2007**, *164* (2), 472–480.
- (14) (a) Lee, Y. H.; Lee, G.; Shim, J. H.; Hwang, S.; Kwak, J.; Lee, K.; Song, H.; Park, J. T. Monodisperse PtRu nanoalloy on carbon as a high-performance DMFC catalyst. *Chem. Mater.* **2006**, *18* (18), 4209–

4211. (b) Koenigsmann, C.; Zhou, W. P.; Adzic, R. R.; Sutter, E.; Wong, S. S. Size-dependent enhancement of electrocatalytic performance in relatively defect-free, processed ultrathin platinum nanowires. *Nano Lett.* **2010**, *10* (8), 2806–2811. (c) Mazumder, V.; Sun, S. H. Oleylamine-mediated synthesis of Pd nanoparticles for catalytic formic acid oxidation. *J. Am. Chem. Soc.* **2009**, *131* (13), 4588–4589.
- (15) (a) Chen, W.; Kim, J. M.; Sun, S. H.; Chen, S. W. Electrocatalytic reduction of oxygen by FePt alloy nanoparticles. *J. Phys. Chem. C* **2008**, *112* (10), 3891–3898. (b) Chen, W.; Kim, J. M.; Xu, L. P.; Sun, S. H.; Chen, S. W. Langmuir–Blodgett thin films of Fe₂₀Pt₈₀ nanoparticles for the electrocatalytic oxidation of formic acid. *J. Phys. Chem. C* **2007**, *111* (36), 13452–13459.
- (16) Hummers, W. S.; Offeman, R. E. Preparation of graphitic oxide. *J. Am. Chem. Soc.* **1958**, *80* (6), 1339–1339.
- (17) Li, D.; Muller, M. B.; Gilje, S.; Kaner, R. B.; Wallace, G. G. Processable aqueous dispersions of graphene nanosheets. *Nat. Nanotechnol.* **2008**, *3* (2), 101–105.
- (18) Ai, K. L.; Liu, Y. L.; Lu, L. H.; Cheng, X. L.; Huo, L. H. A novel strategy for making soluble reduced graphene oxide sheets cheaply by adopting an endogenous reducing agent. *J. Mater. Chem.* **2011**, *21* (10), 3365–3370.
- (19) Chen, W.; Davies, J. R.; Ghosh, D.; Tong, M. C.; Konopelski, J. P.; Chen, S. W. Carbene-functionalized ruthenium nanoparticles. *Chem. Mater.* **2006**, *18* (22), 5253–5259.
- (20) (a) Yuan, Q.; Zhou, Z. Y.; Zhuang, J.; Wang, X. Pd–Pt random alloy nanocubes with tunable compositions and their enhanced electrocatalytic activities. *Chem. Commun.* **2010**, *46* (9), 1491–1493. (b) Guo, S. J.; Dong, S. J.; Wang, E. K. Three-dimensional Pt-on-Pd bimetallic nanodendrites supported on graphene nanosheet: Facile synthesis and used as an advanced nanoelectrocatalyst for methanol oxidation. *ACS Nano* **2010**, *4* (1), 547–555.
- (21) Lu, Y. Z.; Jiang, Y. Y.; Wei, W. T.; Wu, H. B.; Liu, M. M.; Niu, L.; Chen, W. Novel blue light emitting graphene oxide nanosheets fabricated by surface functionalization. *J. Mater. Chem.* **2012**, *22* (7), 2929–2934.
- (22) Huang, J. C.; Liu, Z. L.; He, C. B.; Gan, L. M. Synthesis of PtRu nanoparticles from the hydrosilylation reaction and application as catalyst for direct methanol fuel cell. *J. Phys. Chem. B* **2005**, *109* (35), 16644–16649.
- (23) Kim, C.; Kim, S. S.; Yang, S.; Han, J. W.; Lee, H. In situ shaping of Pt nanoparticles directly overgrown on carbon supports. *Chem. Commun.* **2012**, *48* (51), 6396–6398.
- (24) Zhang, J.; Fang, J. Y. A general strategy for preparation of Pt 3d-transition metal (Co, Fe, Ni) nanocubes. *J. Am. Chem. Soc.* **2009**, *131* (51), 18543–18547.
- (25) (a) Huang, X. Q.; Tang, S. H.; Mu, X. L.; Dai, Y.; Chen, G. X.; Zhou, Z. Y.; Ruan, F. X.; Yang, Z. L.; Zheng, N. F. Freestanding palladium nanosheets with plasmonic and catalytic properties. *Nat. Nanotechnol.* **2011**, *6* (1), 28–32. (b) Kang, Y. J.; Ye, X. C.; Murray, C. B. Size- and shape-selective synthesis of metal nanocrystals and nanowires using CO as a reducing agent. *Angew. Chem., Int. Ed.* **2010**, *49* (35), 6156–6159. (c) Dai, Y.; Mu, X. L.; Tan, Y. M.; Lin, K. Q.; Yang, Z. L.; Zheng, N. F.; Fu, G. Carbon monoxide-assisted synthesis of single-crystalline Pd tetrapod nanocrystals through hydride formation. *J. Am. Chem. Soc.* **2012**, *134* (16), 7073–7080.
- (26) (a) Strmcnik, D. S.; Tripkovic, D. V.; van der Vliet, D.; Chang, K. C.; Komanicky, V.; You, H.; Karapetrov, G.; Greeley, J.; Stamenkovic, V. R.; Markovic, N. M. Unique activity of platinum adislands in the CO electrooxidation reaction. *J. Am. Chem. Soc.* **2008**, *130* (46), 15332–15339. (b) Lee, S. W.; Chen, S. O.; Sheng, W. C.; Yabuuchi, N.; Kim, Y. T.; Mitani, T.; Vescovo, E.; Shao-Horn, Y. Roles of surface steps on Pt nanoparticles in electro-oxidation of carbon monoxide and methanol. *J. Am. Chem. Soc.* **2009**, *131* (43), 15669–15677.
- (27) Mayrhofer, K. J. J.; Juhart, V.; Hartl, K.; Hanzlik, M.; Arenz, M. Adsorbate-induced surface segregation for core–shell nanocatalysts. *Angew. Chem., Int. Ed.* **2009**, *48* (19), 3529–3531.
- (28) (a) Vaseem, M.; Lee, K. M.; Hong, A. R.; Hahn, Y. B. Inkjet printed fractal-connected electrodes with silver nanoparticle ink. *ACS Appl. Mater. Interfaces* **2012**, *4* (6), 3300–3307. (b) Zhao, T.; Sun, R.; Yu, S. H.; Zhang, Z. J.; Zhou, L. M.; Huang, H. T.; Du, R. X. Size-controlled preparation of silver nanoparticles by a modified polyol method. *Colloids Surf., A* **2010**, *366* (1–3), 197–202.
- (29) Xian, J. Y.; Hua, Q.; Jiang, Z. Q.; Ma, Y. S.; Huang, W. X. Size-dependent interaction of the poly(N-vinyl-2-pyrrolidone) capping ligand with Pd nanocrystals. *Langmuir* **2012**, *28* (17), 6736–6741.
- (30) Lu, Y. Z.; Wang, Y. C.; Chen, W. Silver nanorods for oxygen reduction: Strong effects of protecting ligand on the electrocatalytic activity. *J. Power Sources* **2011**, *196* (6), 3033–3038.
- (31) Guo, S. J.; Sun, S. H. FePt nanoparticles assembled on graphene as enhanced catalyst for oxygen reduction reaction. *J. Am. Chem. Soc.* **2012**, *134* (5), 2492–2495.
- (32) Xing, Y. C. Synthesis and electrochemical characterization of uniformly-dispersed high loading Pt nanoparticles on sonochemically-treated carbon nanotubes. *J. Phys. Chem. B* **2004**, *108* (50), 19255–19259.
- (33) (a) Wu, Y. N.; Liao, S. J.; Liang, Z. X.; Yang, L. J.; Wang, R. F. High-performance core–shell PdPt@Pt/C catalysts via decorating PdPt alloy cores with Pt. *J. Power Sources* **2009**, *194* (2), 805–810. (b) Zhou, X. W.; Zhang, R. H.; Zhou, Z. Y.; Sun, S. G. Preparation of PtNi hollow nanospheres for the electrocatalytic oxidation of methanol. *J. Power Sources* **2011**, *196* (14), 5844–5848.
- (34) Sugimoto, W.; Aoyama, K.; Kawaguchi, T.; Murakami, Y.; Takasu, Y. Kinetics of CH₃OH oxidation on PtRu/C studied by impedance and CO stripping voltammetry. *J. Electroanal. Chem.* **2005**, *576* (2), 215–221.